Editors' Suggestion

Measurement of Tunnel Coupling in a Si Double Quantum dot Based on Charge Sensing

Xinyu Zhao[1,2,*] and Xuedong Hu[2,†]

[1] *Department of Physics, Fuzhou University, Fuzhou 350116, China*
[2] *Department of Physics, University at Buffalo, SUNY, Buffalo, New York 14260, USA*

(Received 7 June 2021; revised 10 February 2022; accepted 25 April 2022; published 23 June 2022)

In Si quantum dots, the valley degree of freedom, in particular the generally small valley splitting and the dot-dependent valley-orbit phase, adds complexities to the low-energy electron dynamics. In particular, tunnel coupling, a key knob in charge and spin qubit manipulations, is strongly dependent on the valley-orbit coupling in a Si double dot. Here we propose a four-level model that incorporates excited valley states to extract ground-state tunnel coupling information for a Si double quantum dot. This scheme is based on a charge-sensing measurement on a double dot in equilibrium, as proposed in the widely used protocol for a GaAs double dot [DiCarlo *et al.*, Phys. Rev. Lett. 92, 226801 (2004)]. Our theory helps determine both intra- and intervalley tunnel coupling with high accuracy, and is robust against uncertainties in system parameters such as valley splittings in the individual quantum dots.

DOI: 10.1103/PhysRevApplied.17.064043

I. INTRODUCTION

Tunnel coupling is an essential element in coherent manipulation of electron qubits in semiconductor quantum dots (QDs) [1–18]. It allows single-qubit operations on a charge qubit, and exchange gates for spin qubits [19–25]. Interdot shuttling is also crucial for information transfer on chip [26–33]. With spin and spin-charge hybrid qubits having been demonstrated as hopeful candidates for foundational building blocks of future quantum processors [34–40], accurately characterizing tunnel coupling between quantum dots is an imperative task in characterizing these qubits.

A robust approach to detect tunnel coupling in a double quantum dot (DQD) was developed more than a decade ago [41] based on measuring the charge distribution of the DQD in thermal equilibrium as a function of the interdot detuning and then fitting a two-level (2L) model [42] to obtain the tunnel coupling between the two single-dot ground states. This measurement technique is particularly successful for a GaAs DQD, where excited orbital states are generally about 1 meV or more above the ground state [2,43,44], while experimental temperature is kept at about 100 mK (for a thermal energy of about 10 μeV), safely freezing out orbital excitations, so that the 2L model, including only the single-dot ground states, works perfectly [41,45].

In recent years, studies of spin qubits have focused on Si QDs because of their superior coherence properties [34–40,46]. However, in Si-based QDs, the valley degree of freedom introduces extra energy levels, often only a small fraction of millielectronvolts above the ground states. The availability of such low-energy orbital excitation could be a potential threat to the viability of a spin qubit, though the added freedom could also provide benefits, as illustrated by the hybrid qubit design that is resistant to charge-noise-induced dephasing [19]. The added low-energy valley excited state means that the minimal model to describe charge dynamics in a Si DQD is a four-level (4L) model (see the lower-right inset of Fig. 1) instead of a 2L model, with two relevant tunnel coupling parameters (intra and intervalley) instead of one.

Fitting to a 2L model has been widely used to extract tunnel coupling from charge-sensing measurement at thermal equilibrium in Si quantum dots [47–55]. However, it is an open question whether the 2L model is capable of consistently producing accurate predictions in such measurements. While alternative schemes such as spin-cavity coupling have been employed to successfully measure tunnel coupling [56], the thermal equilibrium charge-sensing technique will still be the most easily accessible and widely used in the foreseeable future. As such, it is important to develop an updated procedure to reliably extract all the tunnel couplings in a Si DQD from these charge-sensing measurements.

In this paper, we apply the 4L model for a Si DQD in the thermal equilibrium charge-sensing measurements of tunnel couplings. Specifically, we develop a numerical 4L

*xzhao@fzu.edu.cn
†xhu@buffalo.edu

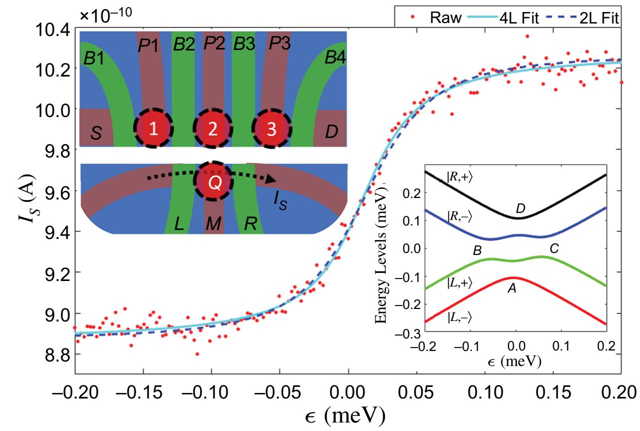

FIG. 1. The $I_S(\epsilon)$ curve measured form experiment (red dots) and the best fit curves. Upper-left inset: schematic diagram of the triple dot configuration. QDs "1, 2, 3" are confined under the plunger gates "$P1$, $P2$, $P3$". Dots "1-2" and "2-3" form two DQD systems. Barrier gates "$B1$" to "$B4$" control the tunneling strength. Dot "Q" plays the role of charge sensor. Lower-right inset: typical energy levels of the DQD.

fitting procedure for both intra and intervalley tunnel couplings of a Si DQD. We also derive a perturbative 4L fitting formula, which speeds up the fitting procedure dramatically while maintaining a high degree of accuracy under most conditions, and allows us to have a better qualitative understanding of the problem. We apply the updated fitting procedures on multiple sets of data obtained in a linear Si/SiGe triple quantum dot (see the schematic diagram in Fig. 1) provided by Adam Mills and Jason Petta [4,49], and produce consistent fitting results. We compare the results from these 4L fitting procedures with the conventional 2L-based approach, and find significant differences under common conditions. For example, in a particular DQD, we observe an average of a 46% difference in the intravalley tunnel coupling between the 2L fitting and 4L fitting. For one set of data, the two models make totally contradictory predictions on tunnel couplings, with the 4L prediction consistent with the experimental procedure and parameters. These examples clearly illustrate the necessity of the 4L model in obtaining a reliable estimate of tunnel couplings in a Si DQD in thermal equilibrium. Lastly, we analyze the robustness of our fitting procedure and identify possible errors.

II. CHARGE DISTRIBUTION IN A FOUR-LEVEL MODEL

The sixfold degeneracy of the Si conduction band is lifted by the growth-direction (nominally the z direction) confinement near an interface, which leaves two of the bulk valleys with lower energy, denoted as $|z\rangle$ and $|\bar{z}\rangle$ states. Scattering at the interface further couples $|z\rangle$ and $|\bar{z}\rangle$ states [15,16,57], leading to the valley eigenstates $|\pm\rangle = (|z\rangle \pm e^{i\phi}|\bar{z}\rangle)/\sqrt{2}$, where the phase ϕ is determined by the interface scattering matrix element. The energy splitting $2|\Delta|$ between $|\pm\rangle$ states is called the valley splitting, and is typically 0.3 to 0.8 meV in a SiMOS quantum dot [58] and up to about 0.3 meV in a Si/SiGe dot (though often closer to 0.1 meV) [13,56,59]. Compared to the few millielectronvolt orbital excitation energy in these quantum dots due to in-plane confinement, valley splitting is much smaller, making it reasonable to neglect intravalley orbital excitation but include both valleys when considering charge distribution in thermal equilibrium at low temperatures.

A minimal model for the low-energy single-electron charge distribution and dynamics of a Si DQD should thus include the ground orbital state in each dot (denoted as $|L\rangle$ and $|R\rangle$ for left and right dots), together with both valley eigenstates, leading to four basis states: $\{|L,+\rangle, |L,-\rangle, |R,+\rangle$, and $|R,-\rangle\}$. Considering that interdot barrier is generally a smooth variation in electrical potential at a length scale much larger than the lattice constant, tunneling is only allowed between states in the same bulk valley: $\langle L,z|H|R,z\rangle = t_C$ is finite while $\langle L,z|H|R,\bar{z}\rangle = 0$. Using the four basis states $|D,\pm\rangle = (|D,z\rangle \pm e^{i\phi_D}|D,\bar{z}\rangle)/\sqrt{2}$ $(D = L,R)$ with local phases ϕ_D, the single-electron Hamiltonian in the Si DQD can be expressed as

$$H = \begin{bmatrix} \epsilon + |\Delta_L| & 0 & t_+ & t_- \\ 0 & \epsilon - |\Delta_L| & t_- & t_+ \\ t_+^* & t_-^* & -\epsilon + |\Delta_R| & 0 \\ t_-^* & t_+^* & 0 & -\epsilon - |\Delta_R| \end{bmatrix}. \tag{1}$$

Here ϵ is the interdot detuning, $|\Delta_{L,R}|$ are the L and R valley splittings, $t_\pm = \frac{1}{2}t_C[1 \pm e^{-i\delta\phi}]$ are the intra- and intervalley (here "valley" means the valley eigenstates $|\pm\rangle$) tunnel couplings, respectively, and $\delta\phi = \phi_L - \phi_R$ is the valley phase difference between the two dots.

Hamiltonian (1) can be numerically diagonalized at any given detuning ϵ to obtain the eigenvalues E_i and the corresponding eigenstates $|\Psi_i\rangle$ $(i = 1,2,3,4)$. It can also be diagonalized analytically, though the general expressions are cumbersome and not transparent. If we treat intervalley tunneling as a perturbation, on the other hand, we can obtain simple analytical expressions for E_i and $|\Psi_i\rangle$ (see Appendix A), which can be used in a fitting procedure much more conveniently. Specifically, the left-dot charge distribution for each eigenstate $|\Psi_i\rangle$ is given by

$$P_{L1} = \cos^2\frac{\Theta_1}{2}\sin^2\frac{\theta_-}{2} + \sin^2\frac{\Theta_1}{2}\cos^2\frac{\theta_+}{2}, \tag{2a}$$

$$P_{L2} = \sin^2\frac{\Theta_2}{2}\cos^2\frac{\theta_-}{2} + \cos^2\frac{\Theta_2}{2}\sin^2\frac{\theta_+}{2}, \tag{2b}$$

$$P_{L3} = \cos^2\frac{\Theta_2}{2}\cos^2\frac{\theta_-}{2} + \sin^2\frac{\Theta_2}{2}\sin^2\frac{\theta_+}{2}, \quad (2c)$$

$$P_{L4} = \sin^2\frac{\Theta_1}{2}\sin^2\frac{\theta_-}{2} + \cos^2\frac{\Theta_1}{2}\cos^2\frac{\theta_+}{2}. \quad (2d)$$

Here $\tan\Theta_1 = |t_-|/(E_+ + E_- + \Delta_+)$, $\tan\Theta_2 = |t_-|/(E_+ + E_- - \Delta_+)$, and $\tan\theta_\pm = |t_+|/(\epsilon \pm \Delta_-)$ ($\theta_\pm \in [0,\pi]$), with $E_\pm = \sqrt{(\epsilon \pm \Delta_-)^2 + |t_+|^2}$ and $\Delta_\pm = \frac{1}{2}(|\Delta_L| \pm |\Delta_R|)$. The expressions given in Eqs. (2) become exact if $|\Delta_L| = |\Delta_R|$. A more detailed study in Appendix B shows that the approximation underlying Eqs. (2) is valid in most regions of the parameter space. For example, even when the valley splittings are significantly asymmetric, $|\Delta_L| = 1.5|\Delta_R|$, there is still only a 5.2% error in the tunnel coupling estimate from the model here compared to direct diagonalization.

When the single electron in the DQD is in thermal equilibrium, its density matrix is given by a thermal state $\rho = \sum_i (1/Z)e^{-\beta E_i}|\Psi_i\rangle\langle\Psi_i|$, where $\beta = 1/k_B T$, k_B is the Boltzmann constant, and $Z = \sum_i e^{-\beta E_i}$ is the partition function. The total charge occupation in the left dot at temperature T is then

$$P_L = \sum_i \frac{1}{Z}e^{-\beta E_i}P_{Li}. \quad (3)$$

Here P_L is a function of both tunnel couplings $t_\pm$, both valley splittings $|\Delta_L|$ and $|\Delta_R|$ (with their phase difference $\delta\phi$ already contained in $t_\pm$), and detuning ϵ. Given experimentally measured $P_L(\epsilon)$, we could thus obtain $t_\pm$ via data fitting. In theory one could obtain the valley splittings from this fitting procedure as well, though our numerical studies below show that the results are not particularly sensitive to $|\Delta_{L,R}|$, making the information obtained from fitting less reliable. Thus we generally treat valley splittings as known parameters.

There are two major reasons that cause different predictions between 2L and 4L theories. First, the different number of levels involved means that the thermal occupations are distributed differently. The impact of this thermal occupation is typically limited since experimental temperature is usually about 100 mK and much smaller than valley splittings in the dots. Obvious exceptions include cases when the valley splittings are very small (for example, about 10 μeV, similar to the thermal energy), or when the temperature is much higher than usual. Second, and more importantly, all eigenstates $|\Psi_i\rangle$ in a Si DQD contain the valley excited states $|+\rangle$ due to the finite intervalley tunnel coupling. The involvement of the excited valley states causes subtle changes to the state compositions, which then lead to differences in the charge distribution.

In the absence of intervalley tunneling ($\delta\phi = 0$), the two valley eigenstates decouple into their own subspaces, so that the charge distribution is reduced to an exact analogy to the 2L case in GaAs when we neglect the thermal occupation of the excited valley states

$$P_L = \frac{1}{2}\left[1 - \frac{\epsilon - \Delta_-}{2E_+}\tanh\left(\frac{E_+}{2k_B T}\right)\right]. \quad (4)$$

This is just the fitting formula in Ref. [41] with an ϵ shift caused by asymmetric valley splittings. If we impose a further condition that the valley splittings are symmetric ($\Delta_- = 0$), the thermal occupation of the excited valley states would have the same left-right distribution as the ground valley states, so that the 4L theory we develop here would become identical to the conventional 2L model. In other words, under the conditions that

$$\delta\phi = 0 \quad \text{and} \quad |\Delta_L| = |\Delta_R|, \quad (5)$$

Eqs. (2) and (3) would lead exactly to the 2L fitting formula in Ref. [41], as is shown in Eq. (4). Note that condition (5) requires symmetric valley splittings. More importantly, whether the two valley splittings are equal is also an important characteristics of any Si DQD. Thus, in Appendix C we point out one way to detect asymmetric valley splittings based on charge sensing. The basic idea is to measure two $P_L(\epsilon)$ curves at different temperatures, and observe whether the intersection of the two curves is located at $P_L = 0.5$.

Direct numerical diagonalization of Hamiltonian (1) can be easily performed by modern computers. On the other hand, the fitting formulae in Eqs. (2) do shed some light on the differences between the 2L and 4L models. The analytical formulae allow us to better quantify how the two models are different, and when they may approach each other in finding $|t_+|$. In Sec. V, we show the condition when the 4L fitting formula is reduced to the 2L case based on an analysis of Eqs. (2). We also clarify the corrections caused by $|t_-|$ in the 4L theory, and the circumstances when 2L fitting produces notable errors. The physical picture behind the formula will be revealed. Last but not least, the fitting formulae of Eqs. (2) do reduce the computational complexity of the problem to some extent, which is beneficial to the real-time automated tuning [49,60–62], providing a more efficient option without sacrificing too much accuracy.

III. EXTRACTING TUNNEL COUPLINGS FROM CHARGE DISTRIBUTIONS

The functional forms for charge distribution in a Si DQD given by Eqs. (2) and (3) allow us to obtain tunnel couplings $t_\pm$ (or t_C and $\delta\phi$) between the two dots by fitting experimentally measured $P_L(\epsilon)$, similar to the procedure given in Ref. [41].

As discussed above, the charge distribution P_L is a function of multiple parameters and variables: $P_L = P_L(\Delta_L, \Delta_R, t_+, t_-, \epsilon)$. To obtain more constrained and reliable knowledge of the tunnel couplings, the valley splittings Δ_L and Δ_R should be known beforehand, for example through the spin relaxation hot spot for each dot [58] or direct spectroscopic measurement [59]. If $|\Delta_{L,R}|$ are not known *a priori*, one can use an estimate instead, without creating significant errors. A detailed discussion of the consequences of not knowing these splittings is given in Appendix G.

Experimentally, either source-drain current I_S or conductance g_S is measured by the charge sensor (for example, a quantum point contact or a single-electron transistor) as a function of the interdot detuning. No matter which quantity is measured, the key is that it has a linear dependence on the charge distribution in the DQD [41]:

$$I_S = I_0 + \delta I\, P_L(\epsilon) + \delta I_{\text{noise}} + \frac{dI}{d\epsilon}\epsilon \tag{6}$$

or

$$g_S = g_0 + \delta g\, P_L(\epsilon) + \delta g_{\text{noise}} + \frac{dg}{d\epsilon}\epsilon. \tag{7}$$

Here I_0 (g_0) is the background current (conductance) setting a reference point, for example, at $\epsilon = 0$, and δI (δg) is the linear conversion ratio between current (conductance) and charge distribution. In addition, the measured interdot detuning ϵ_m may also contain a background voltage, i.e., $\epsilon_m = \epsilon_0 + \epsilon$, where ϵ_m is the experimentally measured value and ϵ_0 is a reference shift. Determining these three reference parameters, I_0, δI, and ϵ_0, is part of the fitting procedure. Furthermore, δI_{noise} (δg_{noise}) is the noise in the I_S (g_S) measurement, and the impact of δI_{noise} will be discussed in Appendix G. The last term $(dI/d\epsilon)\epsilon$ $[(dg/d\epsilon)\epsilon]$ describes the influence on the charge sensor current I_S (conductance g_S) when interdot detuning ϵ is changed. In essence, this term refers to a drift in the charge sensor operating point when the sensed DQD is tuned. While such crosstalk between closely packed gates is unavoidable, we note that recent tuning techniques such as "virtual gates" [4,49,63] have been quite successful in removing such crosstalk and allowing the physical variables of the system and the sensor be controlled independently. Here we do not include this term in our fitting, as we consider the background slope to be too small to cause any significant difference in the fitting results.

Our fitting procedure thus consists of the following steps. First we use Eq. (3) or (4) (for 4L or 2L fitting, respectively) to generate a theoretical curve $I_{\text{th}}(\epsilon)$ with a set of candidate fitting parameters such as $t_\pm$. We then calculate the deviation from the experimental data, and minimize it by varying the fitting parameters. While the three parameters I_0, δI, and ϵ_0 are part of the fitting parameter set, they take up different roles compared to $t_\pm$. The tunnel couplings $t_\pm$ determine the "shape" of the curve, while these three parameters determine the positions of the curve. In particular, ϵ_0 determines the shift in the horizontal (detuning) direction, I_0 determines the vertical shift, while δI is a scaling factor. None of them contributes to the shape or curvature of the curve near $\epsilon = 0$, which is determined by $t_\pm$. Therefore, they can be obtained separately from the main fitting parameters $t_\pm$. One can follow an adaptive fitting procedure that fits these two groups of parameters in turn until they converge to steady values, respectively. A discussion about the fitting inaccuracy caused by errors in I_0, δI, and ϵ_0 can be found in Appendix F, particularly in Fig. 9. Last but not least, we would like to emphasize that the fitting algorithm does not affect the results presented in this paper; our simple and most definitely unoptimized approach obtained a good and reliable fit (see Fig. 7). However, one can certainly use another, hopefully optimized, algorithm based on our formulae to obtain the same results more efficiently.

TABLE I. Best fitting parameters for tunnel couplings. Data sets (a)–(d) are measured from DQD 1-2 with increasing barrier gate voltage V_{B2} and fitted with $|\Delta_L| = 66$ μeV, $|\Delta_R| = 74$ μeV. Data sets (e)–(h) are measured from DQD 2-3 with increasing V_{B3} and fitted with $|\Delta_L| = 74$ μeV, $|\Delta_R| = 74$ μeV. The $|t_\pm|$ units are microelectronvolts. Here (N.) means using numerical diagonalization and (F.) means using Eqs. (2).

DQD 1-2	(a)	(b)	(c)	(d)
2L $\lvert t_+\rvert$	24 ± 0.6	43 ± 1.1	53 ± 1.0	70 ± 2.5
4L $\lvert t_+\rvert$ (N.)	20 ± 1.2	32 ± 1.9	37 ± 2.6	37 ± 6.0
4L $\lvert t_+\rvert$ (F.)	20 ± 1.1	33 ± 1.8	37 ± 2.6	38 ± 5.7
4L $\lvert t_-\rvert$	39 ± 4.7	64 ± 4.8	76 ± 5.9	112 ± 12
4L t_C	44 ± 3.6	72 ± 3.6	85 ± 4.2	118 ± 9.2
4L $\delta\phi$ (rad)	2.2 ± 0.05	2.2 ± 0.03	2.2 ± 0.04	2.5 ± 0.06
DQD 2-3	(e)	(f)	(g)	(h)
2L $\lvert t_+\rvert$	22 ± 0.6	41 ± 0.8	44 ± 0.8	36 ± 1.3
4L $\lvert t_+\rvert$ (N.)	22 ± 0.7	41 ± 1.7	44 ± 1.6	26 ± 2.5
4L $\lvert t_+\rvert$ (F.)	22 ± 0.8	41 ± 1.6	44 ± 1.6	26 ± 2.5
4L $\lvert t_-\rvert$	0 ± 9.6	0 ± 14	0 ± 14	62 ± 7.1
4L t_C	22 ± 3.8	41 ± 4.3	44 ± 4.4	67 ± 5.8
4L $\delta\phi$ (rad)	0 ± 0.22	0 ± 0.20	0 ± 0.18	2.3 ± 0.04

IV. FITTING ACTUAL EXPERIMENTAL DATA: AN EXAMPLE

With the procedure described above, we examine some experimental data acquired during the tune-up of a linear array of nine QDs used to demonstrate charge shuttling [4,33,49]. The measurements are performed on a triple dot schematically shown in Fig. 1. It is part of a Si/SiGe nine-dot array with three sensor dots as charge sensors [4,33,49]. The experimental temperature is $T = 50$ mK [49] and the valley splittings $|\Delta_L|$ and $|\Delta_R|$ are estimated to be around 66–74 μeV from spin measurements in the same device [64]. For each DQD, the $I_S(\epsilon)$ curves are measured with four different barrier gate voltages V_{B2} (or V_{B3}). One set of data, together with our fitting curve, is shown in Fig. 1. All other data sets and fitting curves are shown in Fig. 7 in Appendix D.

Table I summarizes the tunnel couplings and other parameters obtained from the experimental data. In particular, the interdot valley phase difference $\delta\phi$ for QD 1-2 in Table I is roughly a constant under different applied voltages V_{B2}, which implies that varying V_{B2} only changes the interdot barrier height, but does not cause the dots to shift to any significant degree. Consequently, in the 4L model only t_C depends on V_{B2}, while $\delta\phi$ does not.

The various tunnel couplings in Table I are obtained with different fitting formulae. In each subtable, for double dots 1-2 and 2-3, the first row is from a 2L fitting using Eq. (4), labeled as "2L." The second row, together with rows four to six, is from Eq. (3), with a numerical diagonalization of H to calculate P_{Li}, labeled as "4L (N.)." The third row uses the analytical expressions from Eqs. (2) and (3), labeled as "4L (F.)." As the fitting results show, using the analytical expressions from Eqs. (2) lead to almost the same results as numerically diagonalizing the Hamiltonian in these cases. The average difference between 4L $|t_+|$ (F.) and 4L $|t_+|$ (N.) is 0.9%, which indicates that Eqs. (2) are very accurate under these conditions. Additional discussion about the accuracy of Eqs. (2) will be presented in the following sections as well as in Appendix B.

The charge distribution $P_L(\epsilon)$ in the 2L formula (4) depends only on $|t_+|$, and thus only $|t_+|$ can be extracted from a 2L fitting. As shown in Table I, the 2L fitting results are quite different from the 4L results: the average difference between 2L $|t_+|$ and 4L $|t_+|$ for DQD 1-2 is 46% across the different barrier heights in Table I, with the 2L model consistently producing larger tunnel splittings. Qualitatively, this deviation is due to the fact that in the 2L model we are using a single excited level to represent the thermal excitation of three excited levels in the 4L model. As such, this single excited state needs to be above the first excited state but lower than the third excited state in the 4L model. Consequently, $|t_+|$ in the 2L model has to be larger than that in the 4L model. The uncertainties (in Table I) are obtained by numerically generating stochastic realization of δI_{noise} with the same standard deviation as the measured data and then fitting all realizations. Note that the 2L results usually have lower uncertainties as a result of fewer parameters in the simpler model and a less sensitive response to the noisy data. However, the correctness of a fitting model is not determined by its robustness against noise; thus, a robust 2L model is still an inaccurate model with the absence of the intervalley physics, as illustrated by the fact that the difference between the best fits of 4L $|t_+|$ and 2L $|t_+|$ is usually much larger than the uncertainties. Here we assume that the uncertainty mainly

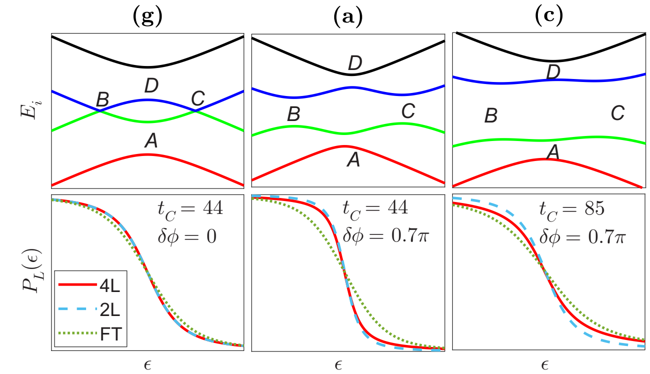

FIG. 2. Theoretically predicted $P_L(\epsilon)$ curves and energy diagrams for DQD with parameters in data sets (g), (a), and (c) of Table I. The curves labeled as "4L" and "2L" are predictions made by Eqs. (3) and (4), respectively (at $T = 50$ mK [49]). The finite-temperature "FT" curves are plotted at $T = 500$ mK using the 4L model. All three columns have the same range in the interdot detuning ϵ along the horizontal axis.

arises from the noise in the I_S signal as shown in Fig. 1, which is the conclusion from Ref. [41] as well.

We tried fitting the experimental data with several combinations of valley splittings $|\Delta_L|$ and $|\Delta_R|$ within the estimated range of 66–74 μeV. The parameters presented in Table I were chosen because they produce the most consistent fitting results for $\delta\phi$. The fitting results for various other combinations of $|\Delta_{L,R}|$ are shown in Fig. 6 in Appendix D, which show that the extraction of $\delta\phi$ from the charge distribution $P_L(\epsilon)$ is quite robust against small variations in the values of valley splittings $|\Delta_{L,R}|$. This robustness probably originates from the fact that variations in this phase difference causes significant changes in the charge distribution with a fixed bulk valley tunnel coupling t_C, as illustrated in Fig. 2 and discussed below.

The best fittings for DQD 2-3 are shown in Table I, data sets (e)–(h). A notable and interesting contradiction arises for data set (h). The 2L theory predicts $t_C = |t_+| = 36$ μeV for data set (h), which is smaller than $t_C = |t_+| = 44$ μeV for data set (g), even though the increase in V_{B3} from data set (g) to (h) should cause the barrier height to decrease and tunnel coupling to increase [64]. This abnormality does not show up in the 4L theory, which suggests that $t_C = 67$ μeV for data set (h), larger than $t_C = 44$ μeV for data set (g). However, the 4L result of $\delta\phi$ for data set (h) is very different from other fitting results for DQD 2-3, as if the dots have shifted so that at least one of the dots has a significantly different valley phase.

Multiple factors could cause such a large change in $\delta\phi$. A real phase shift could occur due to a change in the interface roughness, such as a possible interface step in the DQD [65] when the top gate voltage changes and dots shift. A change in the interface roughness could also lead to significant changes in the valley splitting [52,59,65], introducing another uncontrolled parameter in the measurement. Alternatively, even when there is actually no phase shift, noisy data (see Fig. 7 in Appendix D) or nonlinear effects [41] in Eq. (7) could also cause a spurious change in fitted $\delta\phi$. Without further experimental information, it is impossible to determine the exact reason(s) for the sudden shift in the fitting result for data set (h). Under imperfect conditions, such as a large δI_{noise}, both 2L and 4L theory may fail to provide accurate fitting results. However, it is important to note here that the 2L result is qualitatively wrong since it predicts a larger tunnel coupling for a lower interdot barrier. In Sec. V, we further compare the accuracy of 2L and 4L fittings by numerical experiments.

In an effort to show the consequences of the phase difference $\delta\phi$ and how it affects the charge distribution $P_L(\epsilon)$, we plot the theoretical prediction of the energy spectrum and the corresponding charge distribution $P_L(\epsilon)$ in Fig. 2 by using the parameters of data sets (g), (a), and (c) from Table I. The impact of the phase difference $\delta\phi$ is most clearly demonstrated when comparing data sets (g) and (a), which have almost identical t_C and valley splittings. In data set (g), $\delta\phi = 0$, only intravalley tunneling is allowed, and $t_+ = t_C$. Thus, 2L and 4L predictions overlap with each other in the right panel. With a finite $\delta\phi$ in data set (a), so that $|t_+| < |t_C|$, there is a sharper transition of $P_L(\epsilon)$ near $\epsilon = 0$ (in the middle panel) than there is in data set (g). Namely, the existence of $\delta\phi$ leads to an important quantitative difference in the $P_L(\epsilon)$ curve. The corrections from anticrossings "B" and "C" for data set (a) in Fig. 2 make the 4L curve slightly different from the 2L curve, although in this configuration the correction looks quite small and seemingly insignificant (the reason is discussed later in Sec. V). However, this difference is enhanced when t_C is larger, as shown in the right panel for data set (c). Since the 2L curve represents the case without intervalley tunnel coupling $|t_-|$, the difference between 2L and 4L curves in data set (c) reflects the notable and detectable impact of $|t_-|$. In short, the phase difference $\delta\phi$ (and thus the intervalley tunnel coupling $|t_-|$) can cause an experimentally detectable difference in the shape of the $P_L(\epsilon)$ curve. Last but not least, the contribution of the thermal excitation is mainly determined by the gap $E_2 - E_1$ at lower temperatures. At higher temperatures and when $\delta\phi$ is large, the thermal effect becomes more important as the higher valley excited states are occupied.

The comparison in Table I demonstrates that the simplified and so far widely used 2L model does not accurately extract the tunnel couplings in a Si DQD, and that a more complete model such as the 4L model presented here needs to be used. Qualitatively, the 2L theory only includes the intravalley tunneling that leads to anticrossing "A" in Fig. 1, resulting in a simple form of ground-state charge distribution $P_L = \sin^2(\theta_-/2)$. Four-level theory, on the other hand, accounts for the intervalley tunneling that produces anticrossings "B" and "C" in Fig. 1. These corrections to the 2L theory are represented by the factors $\cos^2(\Theta_1/2)$ and $\sin^2(\Theta_1/2)$ ($|t_-|$ dependent) in Eqs. (2). The details are presented in Appendix A and the magnitude of the 4L corrections from "B" and "C" will be discussed further in the next section.

There are some practical factors that affect the accuracy of the fitting procedure, such as inaccuracies in parameters δI, I_0, ϵ_0, insufficient information of $|\Delta_{L,R}|$, and signal noise in I_S. The impacts of all these factors are discussed in Appendices F and G.

V. CONDITIONS FOR A TWO-LEVEL MODEL

As discussed so far, a 4L model is necessary to provide a thorough and accurate characterization of the low-energy dynamics for an electron in a Si DQD. However, there are situations when t_+ is the only quantity of interest experimentally. A natural question is then whether and when a 2L model can provide reliable information on t_+ based on a charge-sensing measurement. The results summarized in Table I show that 2L fitting sometimes returns quite different values for t_+ from the 4L fitting, while in other cases it does produce results consistent with the 4L model. Here we investigate the differences between the two models in a wide range of experimental conditions (under various $|t_\pm|$, $|\Delta_{L,R}|$, T, etc.), so as to better clarify the applicability of the 2L model in experimental studies of Si DQDs.

To investigate the parameters ($|t_\pm|$, $|\Delta_{L,R}|$, T) in a wider range than the measured ones shown in Table I, we employ Hamiltonian (1) to generate simulated curves of $I_S(\epsilon)$ with a given set of parameters. With this benchmark set, we then apply the procedures we have proposed above to fit such a simulated curve and compare the fitted parameters with the original parameters used to generate the curve. With the true parameters for the "pseudocurve" known as "X_{true}" (X can be $|t_\pm|$, etc.), the "error" of the fitted parameters "X_{fit}" is defined as Error $= (X_{\text{fit}} - X_{\text{true}})/X_{\text{true}} \times 100\%$. Note that the "error" here is different from the inevitable measurement "uncertainty" presented in Table I. The "errors" we discuss in this section refer to deviations from the true values caused by factors such as using different models or using inaccurate input parameters like $|\Delta_{L,R}|$.

We first discuss the necessary condition for a 2L model description of a Si DQD at the low-temperature limit, when the charge distribution $P_L(\epsilon)$ in Eq. (3) is determined by the ground-state charge distribution P_{L1} in Eq. (2a). We have shown in Sec. II and Appendix A that the 2L model for a Si DQD is equivalent to excluding the influence of $|t_-|$, resulting in P_{L1} (for 4L) being reduced to $P_{L1}^{(2\text{L})} = \sin^2(\theta_-/2)$. In the 2L model, $|t_-|$ is treated as 0 so that $\Theta_1 = 0$. Conversely, we can use the magnitude of Θ_1 to characterize the corrections on the 2L model from the 4L model. Recall that $\tan\Theta_1 = |t_-|/(E_+ + E_- + \Delta_+)$ with

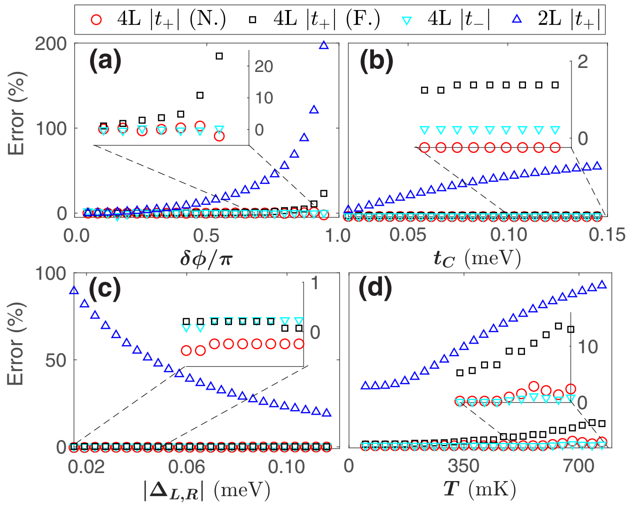

FIG. 3. Errors for different fitting methods. The parameters to generate the "pseudocurve" are $|\Delta_L| = 66$ μeV, $|\Delta_R| = 74$ μeV, $t_C = 71$ μeV, $\delta\phi = 0.7\pi$, and $T = 50$ mK unless specified explicitly in the figures. As shown in the legend, the blue triangles are results from the 2L formula (4), the red circles are obtained via numerical diagonalization of the 4L Hamiltonian, while the black squares are from the 4L analytical formulae of Eqs. (2).

$E_\pm = \sqrt{(\epsilon \pm \Delta_-)^2 + |t_+|^2}$ and $\Delta_\pm = \frac{1}{2}(|\Delta_L| \pm |\Delta_R|)$. Therefore, near $\epsilon = 0$, the ratio $|t_-|/(2\sqrt{\Delta_-^2 + |t_+|^2} + \Delta_+)$ quantifies the correction from the 4L model on the 2L model. As such, under the condition that

$$2\sqrt{\Delta_-^2 + |t_+|^2} + \Delta_+ \gg |t_-|, \tag{8}$$

the 2L model proposed in Ref. [41] should still be a good approximation for describing the ground-state charge distribution of a Si DQD. Particularly, in most cases $|\Delta_L| \approx |\Delta_R|$ and $\Delta_- \approx 0$, so that the condition above can be further simplified as

$$2|t_+| + \Delta_+ \gg |t_-|. \tag{9}$$

Figure 3 provides numerical evidence for condition (8), by exploring how fitting errors depend on the various system parameters. Specifically, Fig. 3(a) shows the effects of $\delta\phi$ with a fixed t_C and valley splittings. Clearly, Eq. (8) is fulfilled when $|t_-| \approx 0$, or, equivalently, $\delta\phi \approx 0$. In this case, the valley states $|+\rangle$ ($|-\rangle$) in the two dots are nearly identical, so that $|\pm\rangle$ in one dot do not tunnel couple to $|\mp\rangle$ in the other dot, and the 4L system is approximately reduced to a pair of 2L systems ($|+\rangle$ and $|-\rangle$, respectively). When $\delta\phi$ (equivalently t_-) is finite, on the other hand, the 2L fitting generally results in significant errors, especially when $\delta\phi \to \pi$. At this limit, condition (8) or (9) would be broken, and the 4L correction is the dominant contribution to ground-state charge distributions.

Figures 3(b)–3(d) show the effects of tunnel coupling t_C, valley splittings $|\Delta_L|$ and $|\Delta_R|$, and temperature. The results are all consistent with condition (8). Here t_C represents tunnel coupling within the same bulk valleys, and is not directly measurable. However, lower tunnel barriers will always lead to larger t_C, and larger t_C always leads to larger $|t_-|$ for a given $\delta\phi$, making the 2L theory less reliable as condition (8) is weakened. Similarly, when $|\Delta_{L,R}|$ is large, the left-hand side of Eq. (8) is larger, making the condition more robust. Consequently, fitting errors by the 2L model are significantly suppressed, as expected. Conversely, when $|\Delta_{L,R}|$ is small, inequality (8) is weakened or even broken, and the 2L theory is less accurate. The large errors of the 2L fitting at higher temperatures are also expected, as there is only one excited state with a simple ϵ dependence, as opposed to three excited states with more complex ϵ dependence.

In the case of charge-sensing measurements at thermal equilibrium for a Si double dot, we would like to emphasize that a 2L theory is never an appropriate starting point, because one cannot obtain valley phase information from single-dot measurements, so that one does not have *a priori* knowledge of whether condition (8) is satisfied. In other words, these tunnel coupling measurements are the first occasion when valley phase is actually relevant to the physical properties of the system. As such, 4L theory should always be the de facto model in these experiments.

It is important to emphasize here again that, while a 2L model may be used to describe a Si DQD under certain conditions, a 4L model is always the more complete description and contains more information. For example, 4L theory automatically extracts intervalley tunnel coupling t_- from the ground-state charge distribution, as shown with the cyan triangles in all four subplots of Fig. 3. We also note that the approximate charge distributions given by the analytical expressions in Eqs. (2) are very accurate except in a very small region when $\delta\phi \approx \pi$ in Fig. 3(a). Therefore, Eqs. (2) are good approximations in most cases, allowing a simpler fitting calculation compared to a fully numerical procedure. A more detailed study on the accuracy of Eqs. (2) is given in Appendix B and Fig. 4.

VI. CONCLUSION

In this paper, we present a 4L model that can extract tunnel coupling information in a Si double quantum dot via measurement of charge distribution of the double dot in thermal equilibrium. In essence, we have adapted the protocol originally proposed and used for a GaAs double dot [41] to a Si DQD by including the valley-orbit coupling and dynamics. We demonstrate the accuracy and robustness of our model and the associated fitting procedure by applying it to experimental data collected in a pair of Si DQDs $I_S(\epsilon)$ [49].

In a Si DQD, valley splittings are generally much smaller than the orbital excitation energy (about 0.1 meV versus about 1 meV), such that a 4L model is usually sufficient to describe the low-energy single electron dynamics theoretically. The practical question is whether a 2L model can properly describe the ground-state tunneling without prior knowledge of valley-orbit coupling in the two dots. Our fitting results clearly demonstrate the discrepancies between the 2L and 4L models, with the 2L model producing an almost 50% larger ground-state tunnel coupling t_+, not to mention that only by the 4L model can one extract any information on the intervalley tunnel coupling t_-. In other words, our results are a clear illustration of the danger in using a 2L model in place of a 4L model to describe the single-electron tunneling in a Si DQD.

In addition to directly diagonalizing the 4L model Hamiltonian numerically in the fitting procedure, we have also derived a set of analytical formulae with the assumption that t_- can be treated perturbatively. Our numerical results show that the approximate formulae perform well in the vast majority of parameter regimes, with the only exception near the point where the interdot valley phase difference is π. We have also compared the performance of the 2L and 4L models, and clarified the condition under which the 2L model could work.

In short, our 4L model for a Si DQD provides thorough and accurate extraction of the intra- and intervalley tunnel couplings t_+ and t_- from a charge distribution measurement, and is important in experimental characterization of single-electron low-energy dynamics in a Si double dot.

ACKNOWLEDGMENTS

This work is supported by the US Army Research Office under Grant No. W911NF1710257 and the Project from Fuzhou University under Grant No. GXRC-21014. The authors thank Adam Mills and Jason Petta for the original data and their helpful discussions. We would also like to thank the valuable comments and suggestions of the reviewers in the reviewing process, which helped us greatly in improving the manuscript.

APPENDIX A: ANALYTICAL CHARGE DISTRIBUTION

In our analytical treatment for a single electron in a Si DQD, we consider intervalley tunnel coupling as a perturbation, while we include intravalley tunnel couplings in the unperturbed Hamiltonian. In essence, we take a DQD with a completely smooth and sharp interface as our starting point. Hamiltonian (1) can thus be split into two parts

$$H = H_0 + H_1, \tag{A1}$$

where

$$H_0 = \begin{bmatrix} \epsilon + |\Delta_L| & 0 & t_+ & 0 \\ 0 & \epsilon - |\Delta_L| & 0 & t_+ \\ t_+^* & 0 & -\epsilon + |\Delta_R| & 0 \\ 0 & t_+^* & 0 & -\epsilon - |\Delta_R| \end{bmatrix}, \tag{A2}$$

$$H_1 = \begin{bmatrix} 0 & 0 & 0 & t_- \\ 0 & 0 & t_- & 0 \\ 0 & t_-^* & 0 & 0 \\ t_-^* & 0 & 0 & 0 \end{bmatrix}. \tag{A3}$$

The eigenenergies and eigenstates of H_0 are

$$E_{1,\pm} = \pm\Delta_+ - E_\pm, \tag{A4}$$

$$E_{2,\pm} = \pm\Delta_+ + E_\pm, \tag{A5}$$

where $E_\pm = \sqrt{(\epsilon \pm \Delta_-)^2 + |t_+|^2}$ and $\Delta_\pm = \frac{1}{2}(|\Delta_L| \pm |\Delta_R|)$, and the corresponding eigenvectors are

$$|\psi_{1,\mp}\rangle = \cos\frac{\theta_\mp}{2}|R,\mp\rangle - e^{-i\delta\phi/2}\sin\frac{\theta_\mp}{2}|L,\mp\rangle, \tag{A6}$$

$$|\psi_{2,\mp}\rangle = \sin\frac{\theta_\mp}{2}|R,\mp\rangle + e^{-i\delta\phi/2}\cos\frac{\theta_\mp}{2}|L,\mp\rangle, \tag{A7}$$

where $\tan\theta_\mp = |t_+|/(\epsilon \mp \Delta_-)$ $(\theta_\mp \in [0,\pi])$.

When the intervalley tunneling $|t_-|$ is finite, Hamiltonian H can be rewritten in the new basis $\{|\psi_{1,\mp}\rangle, |\psi_{2,\mp}\rangle\}$. The matrix representation of H_0 becomes diagonal and the matrix elements of H_1 can be obtained as, for example,

$$\langle\psi_{1,-}|H_1|\psi_{1,+}\rangle = i|t_-|\sin\left(\frac{\theta_-}{2} - \frac{\theta_+}{2}\right), \tag{A8}$$

$$\langle\psi_{1,-}|H_1|\psi_{2,+}\rangle = i|t_-|\cos\left(\frac{\theta_-}{2} - \frac{\theta_+}{2}\right). \tag{A9}$$

When $|\Delta_L| = |\Delta_R|$, $\theta_- = \theta_+$. As a result, $\cos(\theta_-/2 - \theta_+/2) = 1$ and $\sin(\theta_-/2 - \theta_+/2) = 0$. In the new basis $\{|\psi_{1,\mp}\rangle, |\psi_{2,\mp}\rangle\}$, the rotated full Hamiltonian $\tilde{H}$ can be written as

$$\tilde{H} = \begin{bmatrix} -\Delta_+ - E_- & 0 & 0 & i|t_-| \\ 0 & -\Delta_+ + E_- & i|t_-| & 0 \\ 0 & -i|t_-| & \Delta_+ - E_+ & 0 \\ -i|t_-| & 0 & 0 & \Delta_+ + E_+ \end{bmatrix}. \tag{A10}$$

The eigenenergies are then

$$E_1 = \tfrac{1}{2}\left(E_+ - E_- - \sqrt{(E_+ + E_- + 2|\Delta_+|)^2 + |t_-|^2}\right), \tag{A11a}$$

$$E_2 = \tfrac{1}{2}\left(E_- - E_+ - \sqrt{(E_+ + E_- - 2|\Delta_+|)^2 + |t_-|^2}\right), \tag{A11b}$$

$$E_3 = \tfrac{1}{2}\left(E_- - E_+ + \sqrt{(E_+ + E_- - 2|\Delta_+|)^2 + |t_-|^2}\right), \tag{A11c}$$

$$E_4 = \tfrac{1}{2}\left(E_+ - E_- + \sqrt{(E_+ + E_- + 2|\Delta_+|)^2 + |t_-|^2}\right), \tag{A11d}$$

and the corresponding eigenstates are

$$|\Psi_1\rangle = e^{i\phi}\cos\frac{\Theta_1}{2}|\psi_{1,-}\rangle - \sin\frac{\Theta_1}{2}|\psi_{2,+}\rangle, \tag{A12a}$$

$$|\Psi_2\rangle = -e^{i\phi}\sin\frac{\Theta_2}{2}|\psi_{2,-}\rangle + \cos\frac{\Theta_2}{2}|\psi_{1,+}\rangle, \tag{A12b}$$

$$|\Psi_3\rangle = e^{i\phi}\cos\frac{\Theta_2}{2}|\psi_{2,-}\rangle + \sin\frac{\Theta_2}{2}|\psi_{1,+}\rangle, \tag{A12c}$$

$$|\Psi_4\rangle = e^{i\phi}\sin\frac{\Theta_1}{2}|\psi_{1,-}\rangle + \cos\frac{\Theta_1}{2}|\psi_{2,+}\rangle, \tag{A12d}$$

where $\tan\Theta_1 = |t_-|/(E_+ + E_- + \Delta_+)$, $\tan\Theta_2 = |t_-|/(E_+ + E_- - \Delta_+)$, and ϕ is a phase factor with no contribution to probabilities. The left-dot charge distribution $|\langle L,-|\Psi_i\rangle|^2 + |\langle L,+|\Psi_i\rangle|^2$ for these four eigenstates are of the forms given in Eqs. (2).

APPENDIX B: ACCURACY OF THE APPROXIMATE SOLUTION

Eigenstates (A12) are obtained when $|\Delta_L| = |\Delta_R|$. Practically, $|\Delta_L|$ is usually not identical to $|\Delta_R|$. However, the charge distributions in Eqs. (2) remain good approximations. This is because in most cases the nearby dots have similar valley splittings $|\Delta_L| \approx |\Delta_R|$, which makes $\sin(\theta_-/2 - \theta_+/2) \approx 0$. As such, the term $\langle\psi_{1,-}|H_1|\psi_{1,+}\rangle$ that we neglected is generally a small correction compared to $\langle\psi_{1,-}|H_1|\psi_{2,+}\rangle$. Even if $|\Delta_L|$ and $|\Delta_R|$ is quite different, our numerical results in Fig. 4 suggest only a small error in Eqs. (2).

In Fig. 4, we plot the factor $\sin(\theta_-/2 - \theta_+/2)$ under different QD parameters. It shows that in most regions, the factor we have neglected in Eq. (A8) is quite small. Only in the very special case when the phase difference $\delta\phi \to \pi$ and the detuning $\epsilon \to 0$, the factor $\sin(\theta_-/2 - \theta_+/2)$ is notable. Otherwise, Eqs. (2) are always good approximations. Besides, for any $\delta\phi$ and $|\Delta_{L,R}|$, the notable deviation always appears near $\epsilon = 0$. If we consider the average of $\sin(\theta_-/2 - \theta_+/2)$ over all ϵ (because the fitting depends on the charge distribution over all ϵ, not just at $\epsilon = 0$), the average deviation is always small. For a set of practical fitting parameters in Fig. 3, the fitting formulae in Eqs. (2) produce almost identical predictions on both t_+ and t_-. Notable errors only occur at limiting cases, when $\delta\phi \to \pi$ or $k_B T \gg t_C$.

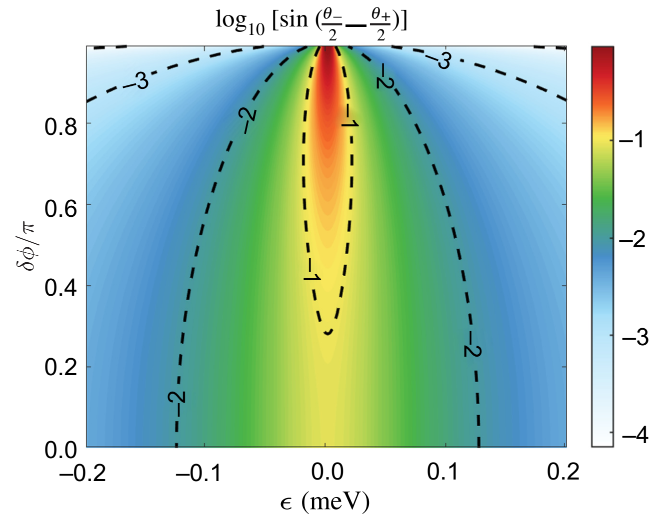

FIG. 4. Accuracy of the approximate diagonalization under different conditions. The parameters are $|\Delta_L| = 66$ μeV, $|\Delta_R| = 74$ μeV, $t_C = 44$ μeV.

We have also performed numerical tests for a large asymmetry in the valley splittings. We use the parameters for data set (a) in Table I, and change $|\Delta_L|$ in the tests. When $|\Delta_L| = 1.5|\Delta_R| = 111$ μeV, the fitting error for t_+ is 5.2%. When $|\Delta_L| = 2|\Delta_R| = 148$ μeV, the fitting error is 8.4%. Therefore, even when there is a 100% difference between the two valley splittings, the fitting error using our formula is still under 10%.

Last but not least, it is straightforward to show that Eqs. (2) always overestimate t_+ compared to the results obtained by numerically diagonalizing the Hamiltonian. Mathematically, this is because we obtain Eq. (A10) by assuming that $\theta_-/2 - \theta_+/2 = 0$. In the general case when $\theta_-/2 - \theta_+/2 \neq 0$, the fitting results would be smaller (albeit only slightly in most cases).

APPENDIX C: DETECTING ASYMMETRIC VALLEY SPLITTINGS

As pointed out in the main text, the measured $P_L(\epsilon)$ curves contain more information than just the tunnel coupling between the lowest two states in the DQD. Here we show that measuring the $P_L(\epsilon)$ curves at two different temperatures can help us determine whether the valley splittings in the two dots are equal, as shown in condition (5). With two different temperatures T_1 and T_2, the two $P_L(\epsilon)$ curves would intersect at $P_L(\epsilon = 0) = 0.5$ if $|\Delta_L| = |\Delta_R|$. According to Eqs. (2), it is straightforward to check when $|\Delta_L| = |\Delta_R|$ and $\epsilon = 0$, $\theta_+ = \theta_- = \pi$, $\sin(\theta_-/2)^2 = \cos(\theta_-/2)^2 = \frac{1}{2}$. Consequently, all the $P_{Li} = \frac{1}{2}$ and P_L in Eq. (3) are independent of T and always 0.5 at $\epsilon = 0$. If

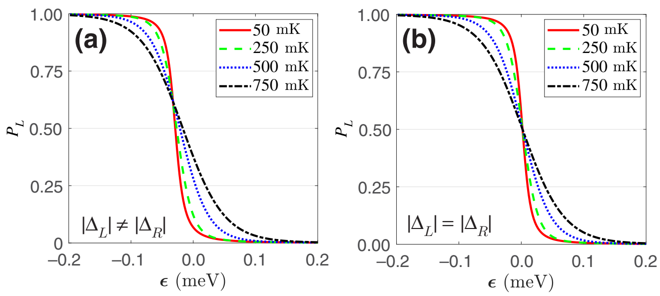

FIG. 5. Interactions of $P_L(\epsilon)$ curves measured at different temperatures. The parameters are $|\Delta_R| = 80\ \mu$eV, $\delta\phi = 0.5\pi$, and $|\Delta_L| = 20\ \mu$eV for (a) and $|\Delta_L| = 80\ \mu$eV for (b).

the valley splittings are asymmetric, on the other hand, $|\Delta_L| \neq |\Delta_R|$, the intersection will be shifted, as shown in Fig. 5. One can thus quickly identify asymmetric valley splittings by observing the intersection of two $P_L(\epsilon)$ curves measured at different T. Note that this is a prediction only possible in 4L theory, while the 2L model always predicts the intersection at $P_L(\epsilon = 0) = 0.5$ because of the absence of valleys.

APPENDIX D: DETAILS OF DATA FITTING

In Sec. IV, the fitting results in Table I are based on a particular choice of valley splittings. In the experiment, the valley splittings $|\Delta_L|$ and $|\Delta_R|$ are not actually measured directly, and are estimated to be around 66–74 μeV [64]. We perform a coarse curve fitting with several groups of $|\Delta_L|$ and $|\Delta_R|$ ranging from 66–74 μeV, as shown in Fig. 6. The data show that, when $|\Delta_L| = 66\ \mu$eV and $|\Delta_R| = 74\ \mu$eV, fitting results of $\delta\phi$ have the smallest standard deviation among data sets (a) to (d). Therefore, we choose this group of valley splittings to perform a fine fitting with higher accuracy and present the results in Table I. We choose this criterion because the only tuned parameter in the experiment is t_C, which would generally not affect $\delta\phi$

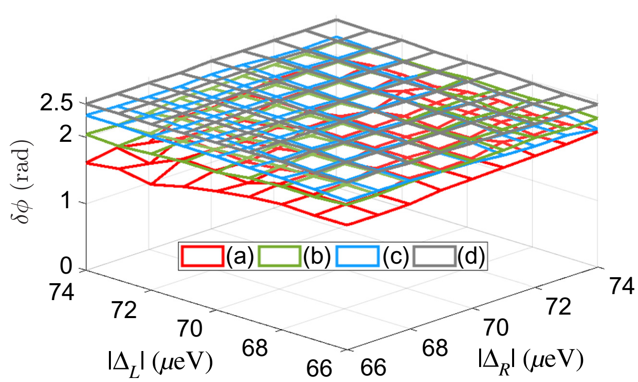

FIG. 6. Fitting results of $\delta\phi$ by using various combinations of $|\Delta_L|$ and $|\Delta_R|$. Four surfaces with different colors are the fitting results from data sets (a)–(d).

when it is not varied too significantly. Interestingly, Fig. 6 shows that other estimates of $|\Delta_L|$ and $|\Delta_R|$ lead to very similar results on $\delta\phi$. Similarly, for data sets (e) to (h), other choices of $|\Delta_{L,R}|$ will not significantly affect the fitting results, too. In short, our fitting procedure does not seem to be overly sensitive to the choices of valley splittings, as long as they are not too different across the two dots.

Besides, we show the raw data and fitting curves of data set (c) in Fig. 1. Here, we show the other seven sets of raw data and the best fitting curves. The raw data are extracted from the readout of the sensor dot directly and the best fitting curves are shown in Fig. 7. For panels (a), (b), and (d), the data are measured from DQD 1-2, with increasing barrier gate voltage V_{B2} (which tunes t_C).

We highlight data set (d) in Fig. 7 because it has the largest t_C, making the difference between the 2L fitting curve and 4L fitting curve clearly observable with the naked eye. One can easily see that the 4L curve fits the raw data better (the numerical standard deviation also proves this). The curve obtained using Eqs. (2) almost coincides with the curve obtained by fully numerical diagonalization, illustrating the robustness of our approximate expressions. Besides, we would also like to emphasize that the actual 2L and 4L fitting results for (d) are quite different (almost 100% according to the results in Table I, much larger than seems from the two curves).

Similarly, the best curve fittings of the data measured from DQD 2-3 are shown in Figs. 7(e)–7(h). The most interesting result is that given in panel (h). Two-level theory predicts t_C(h) to be smaller than t_C(g), while 4L theory suggests that t_C(h) is larger than t_C(g). Experimentally, it is expected that the true value of t_C in panel (h) should be larger because the gate voltage V_{B3} used to tune t_C between dots 2 and 3 is increased from (g) to (h) when the experiment is performed. Here, Fig. 7(h) shows that this set of data is obviously measured with a notably larger noise than other sets. This large noise leads to more significant error for the fitting results. However, we also see that even with such a large noise the 4L fitting still makes a prediction that does not contradict the experimental setup.

APPENDIX E: CORRECTIONS FROM THE 4L MODEL

In Sec. V, we have shown the difference between the 2L and 4L models. Here, we provide more information about the corrections from the 4L model with various QD parameters. It is shown in Fig. 8 that the 4L correction increases with increasing t_C and $\delta\phi$, and decreases with increasing $|\Delta_{L,R}|$. Since the analytical expression $\tan\Theta_1 = |t_-|/(E_+ + E_- + \Delta_+)$ is given in Sec. II, the weak 4L correction in the large $|\Delta_{L,R}|$ region is implied in a straightforward manor. It is worth noting that the 4L correction becomes significant with increasing t_C.

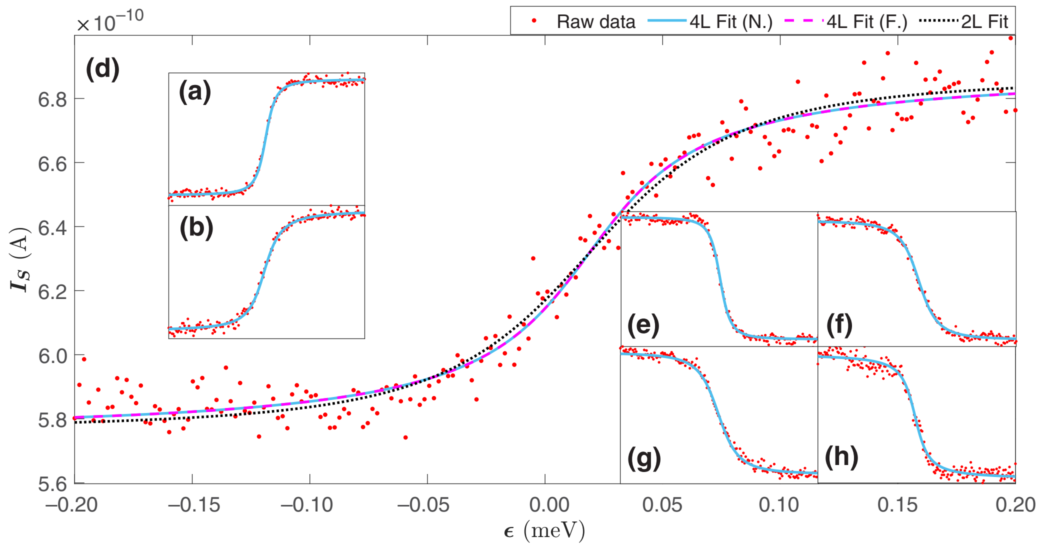

FIG. 7. Curve fitting for actual data measured in the experiment. The results shown in insets (a) and (b) and main plot (d) are obtained from the left two dots (dots 1 and 2) with different barrier gate voltages. The results shown in insets (e)–(h) are measured from the right two dots (dots 2 and 3). Data set (c) is absent since it is presented in Fig. 1.

Increasing the global tunnel coupling t_C leads to increasing both the intra- and intervalley tunnel couplings $|t_+|$ and $|t_-|$, but keeps the ratio $|t_+|/|t_-|$ fixed. In the limit $t_C \to \infty$, $\tan\Theta_1 \to |t_+|/|t_-|$, and this ratio is determined by $\delta\phi$.

APPENDIX F: ESTIMATION OF FITTING PARAMETERS I_0, δI, AND ϵ_0

In Sec. III, we described our fitting procedure by splitting the fitting parameters into two groups: (1) I_0, δI, and ϵ_0, which determine the position of the fitting curve; and (2) t_+ and t_-, which determine the shape of the curve. In our protocol we fit the two groups of parameters in turn until the results converge. Practically, we only perform the iterative fitting for two rounds because bad estimates on I_0, δI, and ϵ_0 do not result in too much error on the final fitting results of $t_\pm$. In Fig. 9, we plot the fitting error caused by incorrect estimates of I_0, δI, and ϵ_0. Figure 9 is plotted in a relative wide range. However, practically, the errors cannot be too large; otherwise, the best fitting curve will have a notable shift. Therefore, the iterative fitting converges very fast and two rounds of fitting is generally enough.

We would like to emphasize that by tuning $t_C = 0$, the parameters can be independently fitted from a calibration procedure prior to the charge-sensing measurement of $|t_\pm|$. Besides, even if the calibration is not performed, I_0, δI, and ϵ_0 are not necessarily obtained by our fitting algorithm (fit them separately). One can certainly use other algorithms based on the 4L model presented in Sec. II.

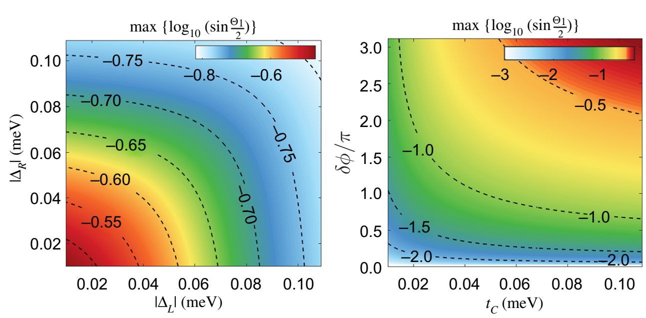

FIG. 8. The corrections from the 4L model indicated by $\sin(\Theta_1/2)$. The maximum value is taken over different values of ϵ.

APPENDIX G: FITTING ERROR CAUSED BY INCOMPLETE KNOWLEDGE OF SYSTEM PARAMETERS

Valley parameters such as $|\Delta_L|$, $|\Delta_R|$ are crucial in describing a Si DQD. As shown in Eqs. (2) and (3), the fitting protocol in our model requires a preliminary measurement on the valley splitting of the two dots. Practically, the valley splittings may be unknown or only roughly estimated. In the example in Table I, the valley splittings are indeed estimated but not measured. It is thus important to know the impact on the accuracy of $t_\pm$ by inexact knowledge of $|\Delta_{L,R}|$.

In Fig. 10 we plot the error caused by incomplete knowledge of valley splittings $|\Delta_{L,R}|$. The numerical data used in the fitting are generated with $|\Delta_{L,R}| = 74$ μeV. We then vary $|\Delta_L|$ or $|\Delta_R|$ on purpose to examine the sensitivity of our protocol to this systematic error.

The numerical results show that a moderate off estimate of $|\Delta_{L,R}|$ will not lead to sizable errors in 4L

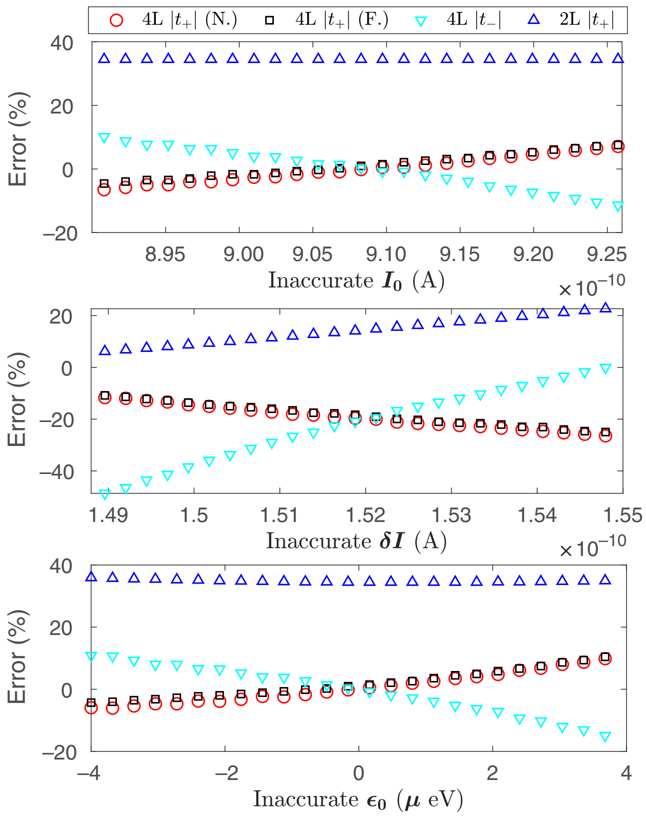

FIG. 9. Fitting error caused by incorrect estimations of I_0, δI, and ϵ_0. Parameters are the same as Table I, data set (b).

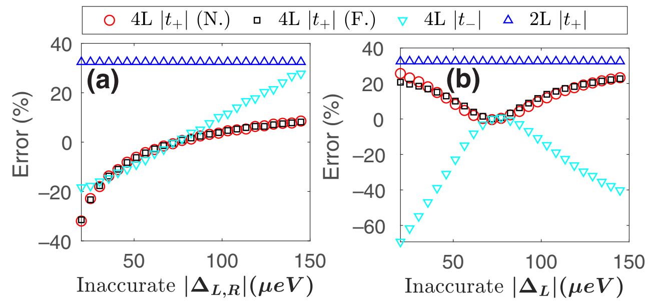

FIG. 10. Fitting error by different methods; the "pseudocurve" data are obtained with $t_C = 71\ \mu$eV, $|\Delta_L| = |\Delta_R| = 74\ \mu$eV, and $\delta\phi = 0.7\pi$. Inaccurate $|\Delta_{L,R}|$ indicate an incorrect estimation or measurement on $|\Delta_{L,R}|$. In (a), we assume that $|\Delta_L| = |\Delta_R|$. In (b), we assume that $|\Delta_R|$ is measured accurately, and that only $|\Delta_L|$ has an error.

fitting unless $|\Delta_{L,R}|$ are significantly underestimated. In Fig. 10(a), when $|\Delta_{L,R}| \approx 37\ \mu$eV (50% underestimated), the 4L fitting error is still only about 10%. Furthermore, overestimated $|\Delta_{L,R}|$ will result in even smaller error compared to underestimated $|\Delta_{L,R}|$, and the 4L fitting error is always smaller than the 2L fitting. Panel (b) shows the case that only one valley splitting ($|\Delta_L|$) is known inaccurately. Similar to panel (a), the 4L fitting error is always smaller than the 2L fitting. We note that the fitting accuracy of intervalley tunnel coupling $|t_-|$ is more sensitive to the knowledge of $|\Delta_L|$, though information on t_- is not accessible at all to a 2L model, since valley physics is not included there.

Another source of error in tunnel couplings is the measurement of the current I_S, which always contains some noise $\delta I_{\mathrm{noise}}$, as shown in Eq. (7) and illustrated in Fig. 1. Here, we use a stochastic function $\delta I_{\mathrm{noise}}$ to simulate the uncertainty in current measurement. The stochastic function is characterized by the mean $\langle \delta I_{\mathrm{noise}} \rangle = 0$ and the standard deviation $\sigma(\delta I_{\mathrm{noise}})$, which indicates the strength of the noise. Numerical results presented in Table II show that the noise $\delta I_{\mathrm{noise}}$ has a much smaller impact on the performance of 2L fitting compared to 4L fitting. Although 2L fitting always produces a significant error over 35%, the error does not change dramatically as $\sigma(\delta I_{\mathrm{noise}})$ increases. As a comparison, the 4L model is more sensitive to noise. The errors from 4L fitting do increase rapidly with increasing $\sigma(\delta I_{\mathrm{noise}})$, but we also note that even when the relative strength of the noise reaches 5%, the 4L fitting error is still under 10%.

TABLE II. Fitting error caused by noise on I_S measurement.

$\sigma(\delta I_{\mathrm{noise}})/\delta I$	0.01	0.02	0.03	0.04	0.05
Error on $|t_+|$ (2L)	36.87%	36.53%	36.18%	36.82%	37.18%
Error on $|t_+|$ (4L)	1.56%	4.30%	4.98%	6.25%	8.19%
Error on $|t_-|$ (4L)	1.06%	2.81%	3.54%	4.16%	4.68%

[1] F. A. Zwanenburg, A. S. Dzurak, A. Morello, M. Y. Simmons, L. C. L. Hollenberg, G. Klimeck, S. Rogge, S. N. Coppersmith, and M. A. Eriksson, Silicon quantum electronics, Rev. Mod. Phys. **85**, 961 (2013).

[2] R. Hanson, L. P. Kouwenhoven, J. R. Petta, S. Tarucha, and L. M. K. Vandersypen, Spins in few-electron quantum dots, Rev. Mod. Phys. **79**, 1217 (2007).

[3] M. J. Gullans and J. R. Petta, Coherent transport of spin by adiabatic passage in quantum dot arrays, Phys. Rev. B **102**, 155404 (2020).

[4] A. Mills, D. Zajac, M. Gullans, F. Schupp, T. Hazard, and J. Petta, Shuttling a single charge across a one-dimensional array of silicon quantum dots, Nat. Commun. **10**, 1 (2019).

[5] J. R. Petta, H. Lu, and A. C. Gossard, A coherent beam splitter for electronic spin states, Science **327**, 669 (2010).

[6] R. M. Otxoa, A. Chatterjee, S. N. Shevchenko, S. Barraud, F. Nori, and M. F. Gonzalez-Zalba, Quantum interference capacitor based on double-passage Landau-Zener-Stückelberg-Majorana interferometry, Phys. Rev. B **100**, 205425 (2019).

[7] M. Kervinen, J. E. Ramírez-Muñoz, A. Välimaa, and M. A. Sillanpää, Landau-Zener-Stückelberg Interference in a Multimode Electromechanical System in the Quantum Regime, Phys. Rev. Lett. **123**, 240401 (2019).

[8] N. E. Penthorn, J. S. Schoenfield, J. D. Rooney, L. F. Edge, and H. Jiang, Two-axis quantum control of a fast valley qubit in silicon, npj Quantum Inf. **5**, 1 (2019).
[9] B. Joecker, P. Cerfontaine, F. Haupt, L. R. Schreiber, B. E. Kardynał, and H. Bluhm, Transfer of a quantum state from a photonic qubit to a gate-defined quantum dot, Phys. Rev. B **99**, 205415 (2019).
[10] X. Zhang, H.-O. Li, G. Cao, M. Xiao, G.-C. Guo, and G.-P. Guo, Semiconductor quantum computation, Natl. Sci. Rev. **6**, 32 (2019).
[11] E. Cota and S. E. Ulloa, Spin–orbit interaction and controlled singlet–triplet dynamics in silicon double quantum dots, J. Phys.: Condens. Matter **30**, 295301 (2018).
[12] F. Martins, F. K. Malinowski, P. D. Nissen, S. Fallahi, G. C. Gardner, M. J. Manfra, C. M. Marcus, and F. Kuemmeth, Negative Spin Exchange in a Multielectron Quantum Dot, Phys. Rev. Lett. **119**, 227701 (2017).
[13] J. S. Schoenfield, B. M. Freeman, and H. Jiang, Coherent manipulation of valley states at multiple charge configurations of a silicon quantum dot device, Nat. Commun. **8**, 64 (2017).
[14] B.-B. Chen, B.-C. Wang, G. Cao, H.-O. Li, M. Xiao, G.-C. Guo, H.-W. Jiang, X. Hu, and G.-P. Guo, Spin blockade and coherent dynamics of high-spin states in a three-electron double quantum dot, Phys. Rev. B **95**, 035408 (2017).
[15] D. Culcer, X. Hu, and S. Das Sarma, Interface roughness, valley-orbit coupling, and valley manipulation in quantum dots, Phys. Rev. B **82**, 205315 (2010).
[16] D. Culcer, Ł. Cywiński, Q. Li, X. Hu, and S. Das Sarma, Quantum dot spin qubits in silicon: Multivalley physics, Phys. Rev. B **82**, 155312 (2010).
[17] Q. Li, Ł. Cywiński, D. Culcer, X. Hu, and S. Das Sarma, Exchange coupling in silicon quantum dots: Theoretical considerations for quantum computation, Phys. Rev. B **81**, 085313 (2010).
[18] X. Li, E. Barnes, J. P. Kestner, and S. Das Sarma, Intrinsic errors in transporting a single-spin qubit through a double quantum dot, Phys. Rev. A **96**, 012309 (2017).
[19] Z. Shi, C. B. Simmons, J. R. Prance, J. K. Gamble, T. S. Koh, Y.-P. Shim, X. Hu, D. E. Savage, M. G. Lagally, M. A. Eriksson, M. Friesen, and S. N. Coppersmith, Fast Hybrid Silicon Double-Quantum-Dot Qubit, Phys. Rev. Lett. **108**, 140503 (2012).
[20] T. S. Koh, J. K. Gamble, M. Friesen, M. A. Eriksson, and S. N. Coppersmith, Pulse-Gated Quantum-Dot Hybrid Qubit, Phys. Rev. Lett. **109**, 250503 (2012).
[21] D. Kim, Z. Shi, C. B. Simmons, D. R. Ward, J. R. Prance, T. S. Koh, J. K. Gamble, D. E. Savage, M. G. Lagally, M. Friesen, S. N. Coppersmith, and M. A. Eriksson, Quantum control and process tomography of a semiconductor quantum dot hybrid qubit, Nature **511**, 70 (2014).
[22] G. Cao, H.-O. Li, G.-D. Yu, B.-C. Wang, B.-B. Chen, X.-X. Song, M. Xiao, G.-C. Guo, H.-W. Jiang, X. Hu, and G.-P. Guo, Tunable Hybrid Qubit in a GaAs Double Quantum Dot, Phys. Rev. Lett. **116**, 086801 (2016).
[23] E. Ferraro, M. De Michielis, G. Mazzeo, M. Fanciulli, and E. Prati, Effective Hamiltonian for the hybrid double quantum dot qubit, Quantum Inf. Process. **13**, 1155 (2014).
[24] J. Taylor, H.-A. Engel, W. Dür, A. Yacoby, C. Marcus, P. Zoller, and M. Lukin, Fault-tolerant architecture for quantum computation using electrically controlled semiconductor spins, Nat. Phys. **1**, 177 (2005).
[25] K. Takeda, A. Noiri, J. Yoneda, T. Nakajima, and S. Tarucha, Resonantly Driven Singlet-Triplet Spin Qubit in Silicon, Phys. Rev. Lett. **124**, 117701 (2020).
[26] F. Ginzel, A. R. Mills, J. R. Petta, and G. Burkard, Spin shuttling in a silicon double quantum dot, Phys. Rev. B **102**, 195418 (2020).
[27] B. Buonacorsi, B. Shaw, and J. Baugh, Simulated coherent electron shuttling in silicon quantum dots, Phys. Rev. B **102**, 125406 (2020).
[28] T. Fujita, T. A. Baart, C. Reichl, W. Wegscheider, and L. M. K. Vandersypen, Coherent shuttle of electron-spin states, NPJ Quantum Inf. **3**, 22 (2017).
[29] J. Villavicencio, I. Maldonado, E. Cota, and G. Platero, Spin-orbit effects in a triple quantum dot shuttle, Phys. Rev. B **88**, 245305 (2013).
[30] J. Zhang, L. Greenman, X. Deng, I. M. Hayes, and K. B. Whaley, Optimal control for electron shuttling, Phys. Rev. B **87**, 235324 (2013).
[31] X. Zhao, P. Huang, and X. Hu, Doppler effect induced spin relaxation boom, Sci. Rep. **6**, 23169 (2016).
[32] X. Zhao and X. Hu, Toward high-fidelity coherent electron spin transport in a GaAs double quantum dot, Sci. Rep. **8**, 13968 (2018).
[33] D. M. Zajac, T. M. Hazard, X. Mi, E. Nielsen, and J. R. Petta, Scalable Gate Architecture for a One-Dimensional Array of Semiconductor Spin Qubits, Phys. Rev. Appl. **6**, 054013 (2016).
[34] A. Tyryshkin, J. Morton, S. Benjamin, A. Ardavan, G. Briggs, J. Ager, and S. Lyon, Coherence of spin qubits in silicon, J. Phys.: Condens. Matter **18**, S783 (2006).
[35] H. Bluhm, S. Foletti, I. Neder, M. Rudner, D. Mahalu, V. Umansky, and A. Yacoby, Dephasing time of GaAs electron-spin qubits coupled to a nuclear bath exceeding 200 μs, Nat. Phys. **7**, 109 (2011).
[36] K. D. Petersson, L. W. McFaul, M. D. Schroer, M. Jung, J. M. Taylor, A. A. Houck, and J. R. Petta, Circuit quantum electrodynamics with a spin qubit, Nature **490**, 380 (2012).
[37] A. M. Tyryshkin, S. Tojo, J. J. Morton, H. Riemann, N. V. Abrosimov, P. Becker, H.-J. Pohl, T. Schenkel, M. L. Thewalt, K. M. Itoh, and S. A. Lyon, Electron spin coherence exceeding seconds in high-purity silicon, Nat. Mater. **11**, 143 (2012).
[38] K. Saeedi, S. Simmons, J. Z. Salvail, P. Dluhy, H. Riemann, N. V. Abrosimov, P. Becker, H.-J. Pohl, J. J. L. Morton, and M. L. W. Thewalt, Room-temperature quantum bit storage exceeding 39 minutes using ionized donors in silicon-28, Science **342**, 830 (2013).
[39] M. Veldhorst, J. C. C. Hwang, C. H. Yang, A. W. Leenstra, B. de Ronde, J. P. Dehollain, J. T. Muhonen, F. E. Hudson, K. M. Itoh, A. Morello, and A. S. Dzurak, An addressable quantum dot qubit with fault-tolerant control-fidelity, Nat. Nanotechnol. **9**, 981 (2014).
[40] A. J. Sigillito, R. M. Jock, A. M. Tyryshkin, J. W. Beeman, E. E. Haller, K. M. Itoh, and S. A. Lyon, Electron Spin Coherence of Shallow Donors in Natural and Isotopically Enriched Germanium, Phys. Rev. Lett. **115**, 247601 (2015).

[41] L. DiCarlo, H. J. Lynch, A. C. Johnson, L. I. Childress, K. Crockett, C. M. Marcus, M. P. Hanson, and A. C. Gossard, Differential Charge Sensing and Charge Delocalization in a Tunable Double Quantum Dot, Phys. Rev. Lett. **92**, 226801 (2004).

[42] S. Shevchenko, S. Ashhab, and F. Nori, Landau–Zener–Stückelberg interferometry, Phys. Rep. **492**, 1 (2010).

[43] L. P. Kouwenhoven, D. G. Austing, and S. Tarucha, Few-electron quantum dots, Rep. Prog. Phys. **64**, 701 (2001).

[44] L. P. Kouwenhoven, T. H. Oosterkamp, M. W. S. Danoesastro, M. Eto, D. G. Austing, T. Honda, and S. Tarucha, Excitation spectra of circular, few-electron quantum dots, Science **278**, 1788 (1997).

[45] J. R. Petta, A. C. Johnson, C. M. Marcus, M. P. Hanson, and A. C. Gossard, Manipulation of a Single Charge in a Double Quantum Dot, Phys. Rev. Lett. **93**, 186802 (2004).

[46] J. J. Pla, K. Y. Tan, J. P. Dehollain, W. H. Lim, J. J. Morton, D. N. Jamieson, A. S. Dzurak, and A. Morello, A single-atom electron spin qubit in silicon, Nature **489**, 541 (2012).

[47] H. Eenink, L. Petit, W. Lawrie, J. Clarke, L. Vandersypen, and M. Veldhorst, Tunable coupling and isolation of single electrons in silicon metal-oxide-semiconductor quantum dots, Nano Lett. **19**, 8653 (2019).

[48] A. J. Sigillito, J. C. Loy, D. M. Zajac, M. J. Gullans, L. F. Edge, and J. R. Petta, Site-Selective Quantum Control in an Isotopically Enriched $^{28}\mathrm{Si}/\mathrm{Si}_{0.7}\mathrm{Ge}_{0.3}$ Quadruple Quantum Dot, Phys. Rev. Appl. **11**, 061006 (2019(R)).

[49] A. Mills, M. Feldman, C. Monical, P. Lewis, K. Larson, A. Mounce, and J. R. Petta, Computer-automated tuning procedures for semiconductor quantum dot arrays, Appl. Phys. Lett. **115**, 113501 (2019).

[50] C. B. Simmons, M. Thalakulam, B. M. Rosemeyer, B. J. Van Bael, E. K. Sackmann, D. E. Savage, M. G. Lagally, R. Joynt, M. Friesen, S. N. Coppersmith, and M. A. Eriksson, Charge sensing and controllable tunnel coupling in a Si/SiGe double quantum dot, Nano Lett. **9**, 3234 (2009).

[51] J. Yoneda, W. Huang, M. Feng, C. H. Yang, K. W. Chan, T. Tanttu, W. Gilbert, R. C. C. Leon, F. E. Hudson, K. M. Itoh, A. Morello, S. D. Bartlett, A. Laucht, A. Saraiva, and A. S. Dzurak, Coherent spin qubit transport in silicon, Nat. Commun. **12**, 4114 (2021).

[52] A. M. Jones, E. J. Pritchett, E. H. Chen, T. E. Keating, R. W. Andrews, J. Z. Blumoff, L. A. De Lorenzo, K. Eng, S. D. Ha, A. A. Kiselev, S. M. Meenehan, S. T. Merkel, J. A. Wright, L. F. Edge, R. S. Ross, M. T. Rakher, M. G. Borselli, and A. Hunter, Spin-Blockade Spectroscopy of Si/Si-Ge Quantum Dots, Phys. Rev. Appl. **12**, 014026 (2019).

[53] T. Ota, T. Hayashi, K. Muraki, and T. Fujisawa, Wide-band capacitance measurement on a semiconductor double quantum dot for studying tunneling dynamics, Appl. Phys. Lett. **96**, 032104 (2010).

[54] J. Stehlik, Y. Dovzhenko, J. R. Petta, J. R. Johansson, F. Nori, H. Lu, and A. C. Gossard, Landau-Zener-Stückelberg interferometry of a single electron charge qubit, Phys. Rev. B **86**, 121303(R) (2012).

[55] K. Petersson, C. Smith, D. Anderson, P. Atkinson, G. Jones, and D. Ritchie, Charge and spin state readout of a double quantum dot coupled to a resonator, Nano Lett. **10**, 2789 (2010).

[56] X. Mi, C. G. Péterfalvi, G. Burkard, and J. R. Petta, High-Resolution Valley Spectroscopy of Si Quantum Dots, Phys. Rev. Lett. **119**, 176803 (2017).

[57] T. Ando, A. B. Fowler, and F. Stern, Electronic properties of two-dimensional systems, Rev. Mod. Phys. **54**, 437 (1982).

[58] C. Yang, A. Rossi, R. Ruskov, N. Lai, F. Mohiyaddin, S. Lee, C. Tahan, G. Klimeck, A. Morello, and A. Dzurak, Spin-valley lifetimes in a silicon quantum dot with tunable valley splitting, Nat. Commun. **4**, 2069 (2013).

[59] E. H. Chen, K. Raach, A. Pan, A. A. Kiselev, E. Acuna, J. Z. Blumoff, T. Brecht, M. D. Choi, W. Ha, D. R. Hulbert, M. P. Jura, T. E. Keating, R. Noah, B. Sun, B. J. Thomas, M. G. Borselli, C. A. C. Jackson, M. T. Rakher, and R. S. Ross, Detuning Axis Pulsed Spectroscopy of Valley-Orbital States in Si/Si-Ge Quantum Dots, Phys. Rev. Appl. **15**, 044033 (2021).

[60] J. P. Zwolak, T. McJunkin, S. S. Kalantre, J. P. Dodson, E. R. MacQuarrie, D. E. Savage, M. G. Lagally, S. N. Coppersmith, M. A. Eriksson, and J. M. Taylor, Autotuning of Double-Dot Devices In Situ with Machine Learning, Phys. Rev. Appl. **13**, 034075 (2020).

[61] T. Nakajima, Y. Kojima, Y. Uehara, A. Noiri, K. Takeda, T. Kobayashi, and S. Tarucha, Real-Time Feedback Control of Charge Sensing for Quantum Dot Qubits, Phys. Rev. Appl. **15**, L031003 (2021).

[62] J. Darulová, S. J. Pauka, N. Wiebe, K. W. Chan, G. C. Gardener, M. J. Manfra, M. C. Cassidy, and M. Troyer, Autonomous Tuning and Charge-State Detection of Gate-Defined Quantum Dots, Phys. Rev. Appl. **13**, 054005 (2020).

[63] T. Hensgens, T. Fujita, L. Janssen, X. Li, C. J. V. Diepen, C. Reichl, W. Wegscheider, S. D. Sarma, and L. M. K. Vandersypen, Quantum simulation of a Fermi–Hubbard model using a semiconductor quantum dot array, Nature **548**, 70 (2017).

[64] A. Mills, private communication.

[65] B. Tariq and X. Hu, Effects of interface steps on the valley-orbit coupling in a Si/SiGe quantum dot, Phys. Rev. B **100**, 125309 (2019).